IRANIAN JOURNAL OF CATALYSIS

Effects of strontium and copper substitution on the catalytic performance of $LaCoO_3$ in the combustion of methane: an optimization study

Hamzeh Rezaei Shadegan, Sarah Maghsoodi*, Bijan Ghanavati, Amirhossein Shahbazi Kootenaei, Alireza Azimi

Department of Chemical Engineering, Mahshahr Branch, Islamic Azad University, Mahshahr, Iran

Received 14 Aguest 2020; received in revised form 17 April 2021; accepted 23 April 2021

ABSTRACT

Cobalt-based perovskites containing strontium and copper ($La_{1-x}Sr_xCo_{1-y}Cu_yO_3$) were synthesized by the sol-gel method and characterized by XRD, H_2-TPR, N_2-adsorbtion, XRF and XPS techniques. The XRD results showed that the rhombohedral structure of perovskites was obtained. The activation energy employed to analyze the activities of samples in the combustion of methane was optimized using full factorial design (FD) by considering strontium (x=0, 0.1 and 0.2) and copper (y=0, 0.25 and 0.5) as the input variables. Analysis of Variance (ANOVA) was employed to investigate the obtained data and a $p<0.05$ was considered statistically significant. A second-order quadratic model was developed to calculate the activation energy on the basis of strontium and copper doping-degrees. FD results showed that perovskites containing strontium and copper in the range of 0.07-0.15 and of 0.2-0.4, respectively, had the best catalytic activity owing to the higher surface area, higher amounts of oxygen species, better reducibility and oxygen mobility.

***Keywords**: Methane, Perovskite, Cobalt, Strontium, Copper*

1.Introduction

Methane presents at low concentrations in many fugitive emissions, such as car exhaust gases, and needs further process to prevent pollution. Catalytic combustion is the main process for oxidation of unburned methane. As compared to conventional flame combustion, it needs lower temperatures and accordingly leads to lower emissions of CO and NO_x. Since, conventional flame combustion uses temperatures as high as 1800 °C, a high amount of nitrogen oxides (NO_x) will be formed [1, 2]. Although supported palladium oxide is known to be a very active catalyst for catalytic conversion of hydrocarbons, its application has been limited because of sinterization and deactivation problems. It has been reported that sintering of Pd particles is significant only at 600 °C or above [3]. Furthermore, the high cost of Pd is another obstacle which should be considered [4, 5].
Perovskites are mixed oxides of general formula ABO_3, where A and B are mainly rare earth and transition metal cations respectively [5, 6]. Both A and B can be partially substituted by different kinds of rare earth and transition metals to make perovskite-type oxides of general formula $A_{1-x}A_xB_{1-y}B_yO_3$ [4, 5]. In Perovskite materials, activity is related to B while A is responsible for the formation of crystal lattice and its stability. However, when A is partially substituted by A', it affects the valence state of B which can improve the catalytic activity [4, 7]. Perovskite-type oxides have attracted scientists' attention and are considered as potential substitutes due to high thermal stability and activity.
Among different types of perovskite materials, $LaCoO_3$ has attracted more attention due to its specific oxygen nonstoichiometries which can be further modified through the partial substitution of A- or B-site metal ions [6, 8-10].Many efforts have been made to increase $LaCoO_3$ activity by partial substitution of lanthanum (La) and cobalt (Co) cations [8, 9, 11]. The addition of Cu into $LaCoO_3$ increased its activity in the reduction of NO by CO [12]. Glisenti et al. [13] reported that oxidation ability of $LaCo_{0.5}Cu_{0.5}O_3$ was noticeably

*Corresponding author.
E-mail address: *maghsoodi_mahshahr@yahoo.com*
(**S. Maghsoodi**)

better than that of $LaCoO_3$. Moreover, our previous study demonstrated that incorporation of Ni, Cu and Fe into $LaCoO_3$ increased its catalytic activity in combustion of methane [14]. Partial substitution of Co cations by transition metals such as Cu can change the valency of Co cations and accordingly modify the oxygen mobility and reducibility [9, 15]. For instance, oxygen vacancies can be formed through substituting trivalent Co cation (Co^{3+}) by a bivalent cation (such as Cu^{2+}) due to positive charge deficiencies. Strontium (Sr) is reported as an appropriate candidate to be partially substituted at La sites. For instance, Kim et al. [16] reported that $La_{0.9}Sr_{0.1}CoO_3$ and $La_{0.9}Sr_{0.1}MnO_3$ perovskites had higher NO oxidation activity than Pt-based catalysts. Zhang et al. [17] found that the addition of Strontium into La_2CuO_4 increased its performance in methane oxidation.

According to the literature [9, 15, 17], the addition of Strontium into cobalt based perovskites results in an improvement in catalytic oxidation reactions. Partial substitution of Sr^{+2} at La^{+3} sites in $LaCoO_3$ lattice creates a net charge imbalance that needs to be compensated by oxygen vacancies to keep the charge balanced .It has been found that reducibility and oxygen mobility improved by this phenomenon. On the other hand, recent researches have shown that Cu can make impressive effects on the oxygen mobility of $LaCO_3$. When Co is partially substituted by Cu, the structure of $LaCoO_3$ has to be distorted which causes the appearance of some anionic deficiencies. This phenomenon leads to some transformation in the valence states of Co cations, resulting in the improvement of the catalytic behavior [12, 18].

Consequently, different types of $La_{1-x}Sr_xCo_yCu_{1-y}O_3$ perovskites were synthesized to study the effects of Sr and Cu metals on the catalytic properties of $LaCO_3$. For this purpose, the experimental design of experiments (DoE) was employed to investigate interaction effects of Sr and Cu. The potential for using DoE in data analysis is especially high in the case of systems with nonlinear and interaction effects because DoE possesses the capability to be developed from a set of experimental data without actual knowledge of the physical and chemical laws that govern the system [19, 20]. In this study, nine cobalt-based perovskite-type oxides were synthesized with different amounts of Sr and Cu. The obtained solids were characterized by XRD, BET, H_2-TPR and XPS techniques to investigate physicochemical properties of them. Finally, full factorial design of experiments coupled with response surface methodology were employed to investigate the effects of Sr and Cu on the combustion of methane and optimize Sr and Cu doping degrees in $LaCoO_3$ lattice.

2. Experimental

2.1. Catalyst preparation

$La_{1-x}Sr_xCo_{1-y}Cu_yO_3$ perovskites with x=0, 0.1, 0.2 and y=0, 0.25, 0.5 were synthesized by the citric acid sol-gel method using $La(NO_3)_3.6H_2O$, $Co(NO_3)_2.6H_2O$, $Cu(NO_3)_2{\cdot}3H_2O$, $Sr(NO_3)_2$, citric acid ($C_6H_8O_7$) and ethylene glycol ($C_2H_6O_2$) as the starting materials [12, 21, 22]. All starting synthesis grade materials were supplied by Merck Company. Briefly, appropriate quantities of citric acid, ethylene glycol and a little amount of water were mixed with vigorous stirring to obtain a homogeneous viscous solution. Then, Stoichiometric quantities of $Co(NO_3)_2.6H_2O$ and $Cu(NO_3)_2{\cdot}3H_2O$ were added to the solution and allowed to stir at 65 °C until a clear solution was obtained. Afterward, stoichiometric amounts of $La(NO_3)_3.6H_2O$ and $Sr(NO_3)_2$ were added and allowed to stir at 65 °C until the excess solvents evaporated and a spongy gel was formed. In the next step, the spongy gel was dried at 65 °C for 24h in an oven and finally calcined at 800 °C in the air for 4h.

For all samples, the molar ratios of citric acid/ethylene glycol/total nitrates were kept at 5:5:1 while the molar ratios of total A ions (La+Sr) to total B ions (Co+Cu) were kept at 1:1. The synthesized samples were labeled as SrxCuy where x refers to Sr and y refers to Cu. For instance, $La_{0.9}Sr_{0.1}Co_{0.5}Cu_{0.5}O_3$ was labeled as Sr0.1Cu0.5. The composition of the initial gels for all synthesized samples are given in **Table 1**.

2.2. Catalyst characterization

X-ray diffraction studies were performed using an 1840 Philips diffractometer with Cu Kα radiation (λ = 1.54 Å) in the 2θ range of 20–80 with a step size of 0.02 °/s, to investigate the structure and crystallinity of the samples. The operating voltage and current were 40 kV and 40 mA, respectively.

The surface area and pore volume of the samples were measured by Nitrogen adsorption and desorption experiments at –196 °C using a Micromeritics TriStar 3000 automated system. Before experiments, the samples were first degassed for 2 h at 200 °C to remove moisture. The surface area was calculated by the BET method. X-ray fluorescence (XRF) technique using a Philips PW2404 XRF spectrometer was employed to analyze the elemental composition of the samples.

To investigate the chemical bonding state of the desired elements, X-ray photoelectron spectroscopy (XPS) tests were carried out on a Gammadata-scienta ESCA 200 hemispherical analyzer using an Al Kα (1486.6 eV) X-ray source.

Table 1. Coded and actual values of the variables of the design of experiments

Factor	Variable	Level		
		-1	0	1
A	Cu doping degree (at%)	0	0.25	0.5
B	Sr doping degree (at%)	0	0.1	0.2

The spectra were registered after degassing the samples at ambient temperature under vacuum. The electron binding energies were calibrated by the C 1s hydrocarbon peak at 285 eV as a reference.

Reduction reactivity of the samples was investigated using hydrogen temperature-programmed reduction analysis (H_2-TPR) by a Micrometer 2900 equipped with a thermal conductivity detector (TCD). Each sample was weighted 50 mg and was loaded into a tubular quartz microreactor. The sample was first purged at 300 °C for 1h under a flow of Ar and then cooled to room temperature. Then, H_2-TPR step was conducted in a reducing gas flow of 10% H_2 in Ar with concomitant temperature leveling up to 900 °C with a heating rate of 10 °C /min.

2.3. Evaluation of catalytic performance

Catalytic experiments for the combustion of methane were performed in a fixed bed quartz reactor with an internal diameter of 10 mm and 50 cm length at a temperature ranging from 350 °C to 750 °C under atmospheric pressure. A schematic representation of the set-up is shown in **Scheme 1**.

For all tests, 200 mg catalyst was taken and loaded into the reactor. The total flow rate of the reactant gas with a molar composition of CH_4:O_2:N_2 =2:18:80 was equal to 30 cm^3/min which was controlled by mass flow controllers. The gas phase effluent from the reactor was analyzed online using a Varian CP-3800 gas chromatograph equipped with a flame ionization detector (FID) and a thermal conductivity detector (TCD). The apparatus employed CP-Sil 5CB column and Molsieve 13c to separate the desired components. The activation energy (E) was employed to compare the catalytic activities of the samples.

Calculations of the activation energies were done by assuming a simple first-order reaction rate. Hence, the $\ln(-\ln(1-\alpha)) = (1000/RT)$ dependence was plotted where α, T and R are the conversion of methane, temperature and gas constant, respectively. The activation energies were calculated by the Arrhenius equation based on the slope of the plotted straight line [23, 24].

2.4. Statistical method and data analysis

Effects of Sr and Cu as independent variables on activation energy in the catalytic combustion of methane were investigated using full factorial design of experiments. These variables were identified at three different levels of 0, 0.1 and 0.2 for Sr and 0, 0.25 and 0.5 for Cu. The values were selected based on the results of preliminary experiments. Three factorial levels for each variable were coded as -1, 0 and +1 for low, medium and high using **Eq. (1)** [19, 20].

$$x_i = (X_i - X_{i0}) / \Delta X_i \qquad i = 1, 2, 3, \ldots K \qquad \textbf{(1)}$$

Where x_i is the coded value of i*th* factor, X_i is the actual value of i*th* factor, X_0 is the actual value of X_i at the medium point and ΔX_i is the factor-variation interval. The independent variables with their values in actual and coded form are given in **Table 2**.

In a full factorial design for two variables, a total of 9 runs were required which can be determined using **Eq. (2)**.

$$n_e = 3^k \qquad \textbf{(2)}$$

Where n_e is the total number of experiments and k is the number of independent variables. Behavior of the system as a function of independent variables in this study was expressed by the following second-order polynomial equation:

$$Y = \beta_0 + \sum_{i=1}^{k} \beta_i X_i + \sum_{i=1}^{k} \beta_{ii} X_i^2 + \sum_{i=1}^{k} \sum_{i<j}^{k} \beta_{ij} X_i X_j$$

Where Y is the predicted response, k is the number of independent parameters, β_0 is an intercept coefficient, β_i is a linear term, β_{ii} is a quadratic term, β_{ij} is an interaction term and X_i and X_j are the actual variables.

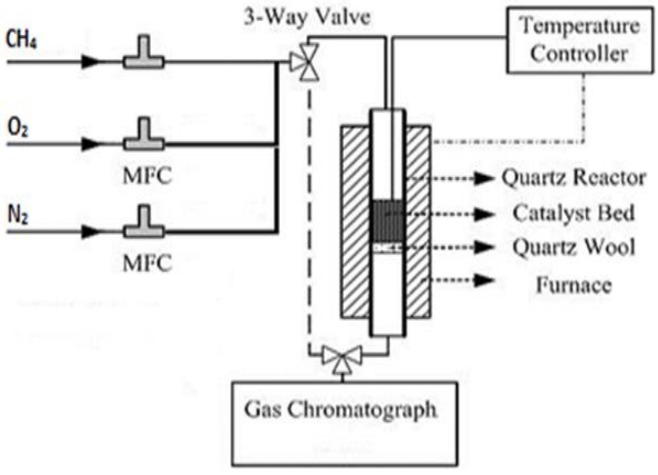

Scheme 1. Schematic representation of the set-up

Table 2. Physical properties and bulk composition of the perovskites

sample	Cell volume (A^3)	BET surface area (m^2/g)	Pore volume (cm^3/g)	Bulk compositiona (at%)			
				La	Sr	Co	Cu
$LaCoO_3$	338.26	9.8	0.09	52.1 (50)[a]	0	47.9 (50)	0
Sr0Cu0.25	339.28	9.1	0.08	51.8 (50)	0	35.4 (37.5)	12.8 (12.5)
Sr0.1Cu0.25	339.32	8.7	0.08	40.8 (40)	9.7 (10)	35.1 (37.5)	14.4 (12.5)
Sr0.2Cu0.25	339.84	7.9	0.06	32.5 (30)	18.2 (20)	35.9 (37.5)	13.4 (12.5)
Sr0.1Cu0	338.37	10.1	0.09	42.3 (40)	9.5 (10)	48.2 (50)	0
Sr0.1Cu0.50	342.56	6.7	0.06	41.8 (40)	9.1 (10)	21.76 (25)	27.34 (25)

[a] Nominal values are in parentheses.

3. Result and Discussion

3.1. Catalyst characterization

3.1.1. XRD

Fig. 1 presents the XRD results of the $La_{0.9}Sr_{0.1}Co_{1-y}Cu_yO_3$ (**Fig. 1a**) and $La_{1-x}Sr_xCo_{0.75}Cu_{0.25}O_3$ (**Fig. 1b**) samples. As a reference, the XRD pattern of $LaCoO_3$ is given in both **Fig. 1a** and **Fig. 1b**. According to **Fig. 1a**, XRD characterization revealed that all $La_{0.9}Sr_{0.1}Co_{1-y}Cu_yO_3$ samples possessed reflex ions ascribed to the rhombohedral $LaCoO_3$ structure (JCPDS card 48-0123). No diffraction peaks related to impurity oxides were observed in Sr0.1Co0 and Sr0.1Co0.25 samples, indicating the formation of the perovskite structure with single phase. However, a trace amount of segregated Cu oxide phases could be detected in the XRD pattern of Sr0.1Co0.5 sample. Later as demonstrated by XPS, a large amount of Cu exited with the oxidation state of Cu^{+2} in the perovskite structure. This phenomenon is attributed to the fact that the ionic radius of Cu^{+2} is larger than Co^{+3}, resulting in the segregation of some CuO when its amount was high [12, 25]. It should be noted that the intensity of the peaks of the X-ray diffraction patterns decreased as the amount of Cu increased which demonstrates the grain size became smaller and crystallinity fallen. Furthermore, the main diffraction peak at 2θ=33° shifted slightly toward the lower angles as more Cu was substituted at Co sites, indicating the appearance of the lattice expansion because of the larger ion radius of Cu^{+2} as compared to Co^{+3} [26]. This can also be seen from the cell volume size in **Table 3**.

Fig. 1b shows that the perovskites with the rhombohedral structure were formed for all $La_{1-x}Sr_xCo_{0.75}Cu_{0.25}O_3$ samples without any impurities. The main characteristic peak around 33° slightly shifted toward higher angles and its intensity decreased as Sr substitution degree increased, indicating a small amount of La^{3+} cations were substituted by Co^{+3} [26]. In addition, a zoom in 2θ between 32° and 35° relating to the most intense diffraction peak of $LaCoO_3$ perovskite shows a splitting characteristic of rhombohedra symmetry. The addition of Sr resulted in the overlapping of both peaks and made an asymmetric wide peak of a distorted rhombohedra (JCPDS card 048-0122) because of the formation of a spinel-type structure [27]. Therefore, a gradual transformation in the characteristic pattern from the rhombohedral structure to the rhombohedral distorted structure happened as Sr content increased.

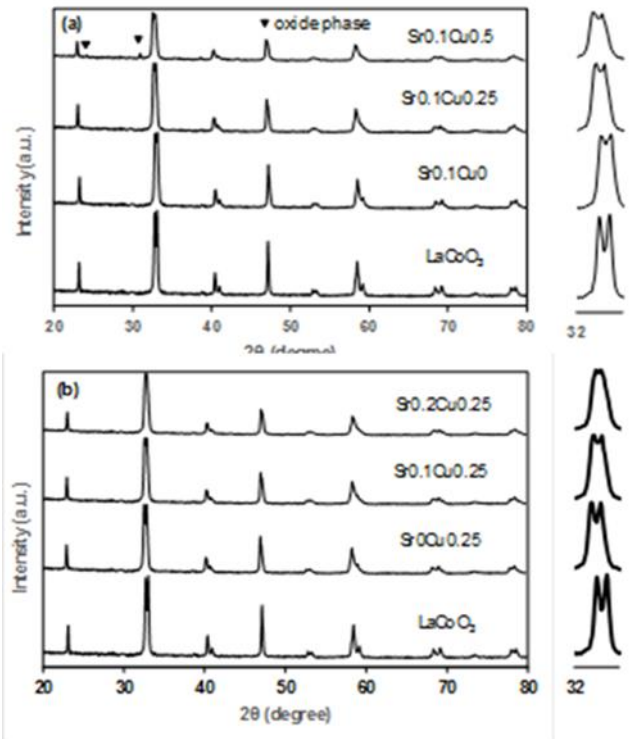

Fig. 1. XRD patterns of (a) Sr0.1Cuy and (b) SrxCu0.25 perovskite samples

Table 3. Surface atomic ratios of different compounds in the perovskites

sample	Surface composition (at%)					
	Sr_{seg}/S_{tot}	Sr/Co	Cu/Co	Cu^{1+}/Cu^{2+}	Co^{2+}/Co^{3+}	O_{ads}/O_{latt}
$LaCoO_3$	-	0 (0)[a]	0 (0)	-	22.1	121.2
Sr0Cu0.25	-	0 (0)	0.38 (0.33)	11.2	18.2	181.5
Sr0.1Cu0.25	0.54	0.33 (0.26)	0.41 (0.33)	16.6	17.5	192.6
Sr0.2Cu0.25	0.63	0.61 (0.53)	0.45 (0.33)	21.2	17.1	198.3
Sr0.1Cu0	0.53	0.30 (0.2)	0 (0)	-	21.4	132.3
Sr0.1Cu0.50	0.61	0.51 (0.4)	1.27 (1)	34.5	15.1	226.1

[a] Nominal values are in parentheses.

3.1.2. Textural and physical properties

The textural and physical properties of synthesized samples including BET surface area, pore volume and bulk elemental composition are given in **Table 3**. $LaCO_3$ had a specific surface area of 9.8 m^2/gr and a total pore volume of 0.09 cm^3/gr. It can be seen that the BET surface area and pore volume of the modified samples are close to $LaCO_3$ and no significant differences were observed after the incorporation of Cu and Sr. The lowest BET surface area and pore volume belonged to Sr0.2Cu0.5, due to the segregation of some CuO oxides which may block the access to the pores [11, 22].

The bulk elemental composition of the samples measured by XRF shows that the real values of the elements are close to theoretical ones. Actually, some little differences can be observed which may be attributed to experimental errors. Another possible explanation is due to formation of some intermediate valence state metal ions during the synthesis process which affects the XRF results [26]. It should be noted that theoretical values are only based on saturated metal ions.

The surface elemental compositions based on XPS are shown in **Table 4**. The ratio of segregated Sr to total Sr was chosen to investigate accommodation capacity of Sr in $LaCoO_3$ lattice. It can be clearly observed that ratio of Sr_{seg}/S_{tot} raised with increasing Sr and Cu doping degrees. For instance, the Sr_{seg}/S_{tot} of the samples increased from 0.54 to 0.63 m^2/g and 0.53 to 0.61 cm^3/g when x and y respectively increased from 0.1 to 0.2 and 0 to 0.5. These phenomena demonstrated that there was a limited capacity for Sr element to be incorporated into $LaCoO_3$ lattice. On the other hand, the real surface ratios of Sr/Co and Cu/Co were higher than the theoretical ones and the differences became more significant as Sr and Cu doping degrees increased. This further confirmed the difficulty of Sr and Cu ions incorporation into $LaCoO_3$ lattice [22].

3.1.3. H_2-TPR

The reduction reactivity of the synthesized samples was investigated by H_2-TPR and acquired results are shown in **Fig. 2**. It should be first noted that La and Sr were not reducible in the range of temperatures studied here [28]. The reduction profiles were divided into two regions, called α-reduction for temperatures below 500 °C and β-reduction for temperatures above 500 °C. In general, the peaks in the α-reduction region are due to the reduction of cation defective sites at oxygen vacancies while the those in the β-reduction region are derived from the reduction of metal species in the bulk of perovskite [17, 23].

In the case of $LaCoO_3$, there were four reduction peaks at temperatures about 370, 420, 585 and 635 °C. According to the literature [26, 27] the two first peaks at temperatures below 500 °C are due to the reduction of Co^{3+} ions to Co^{2+} while the last two are associated with the reduction of Co^{2+} ions to metallic Co in the bulk of the $LaCoO_3$ structure. For $La_{0.9}Sr_{0.1}Co_{1-y}Cu_yO_3$ samples (**Fig. 2a**), a new reduction peak at temperature about 305 °C was detected as the reduction of Cu^{2+} to Cu^+ [12, 17]. The peak at 360 °C arose from the overlapping reduction of Cu^+ to metallic Cu and Co^{3+} to Co^2 and the last peak at temperature 540 °C was associated with the reduction of Co^{2+} ions to metallic Co. it can be observed that the reduction temperatures shifted significantly to lower temperatures in comparison with $LaCoO_3$ which means the presence of Cu in the $LaCoO_3$ structure eased the reducibility of the Co species. On the other hand, the peak area increased as the content of Cu in the $LaCoO_3$ structure enhanced, demonstrating the number of consumed hydrogen moles increased. The more hydrogen consumption, the higher number of reducible species.

The TPR curves for $La_{1-x}Sr_xCo_{0.75}Cu_{0.25}O_3$ samples in **Fig. 2b** show similar trends to those of $La0.9Sr0.1Co1-_yCu_yO_3$ samples with three reduction peaks at about 305, 360 and 540 °C. It can be observed that the enhancement of Sr substitution degree caused the movement of reduction peaks to lower temperatures. Furthermore, the area of the reduction peaks increased as the amount of Sr enhanced. These behaviors demonstrate that the

Table 4. Design matrix and the activation energies for full factorial configuration

Run Number	Sr substitution degree (x)	Cu substitution degree (y)	Activation Energy (kj/mol)
1	0.20	0.25	58.38
2	0.10	0.25	54.02
3	0.20	0.00	62.19
4	0.20	0.50	64.19
5	0.00	0.00	70.48
6	0.10	0.00	60.34
7	0.00	0.50	61.17
8	0.00	0.25	58.85
9	0.10	0.50	58.31

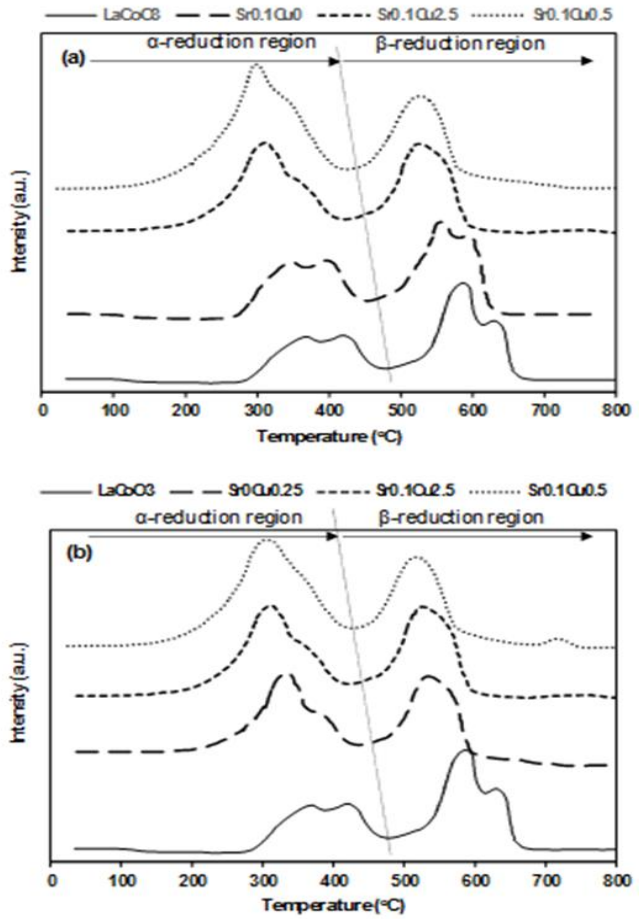

Fig. 2. H_2-TPR profiles of (a) Sr0.1Cuy and (b) SrxCu0.25 perovskite samples.

reduction ability of Co and Cu was facilitated in the presence of Sr ions. As we know, Sr is not reducible in the TPR temperature range, so generation of oxygen vacancies due to the positive charge defects after the substitution of La^{3+} by Sr^{2+} is the only mechanism available to improve the reducibility. In fact, an increase in the area of α-reduction peaks to β-reduction peaks was observed which proves the mentioned mechanism.

3.1.4. XPS investigations

XPS technique was applied to investigate the oxidation state of each element and acquired results for Cu, Sr, Co and O are given in **Figs. 3-6**, respectively.

For Cu 2p in **Fig. 3**, the peaks at 933 eV (Cu $2p_{3/2}$) and 953 eV (Cu $2p_{1/2}$) and their satellite at 942 eV are characteristic of Cu^{2+}. In addition, a little peak at 932.4 eV is detected which is the signal of Cu^{+1}. The results demonstrates that Cu was mainly in the oxidation state of +2 and a small amount of +1 oxidation state co-existed [29]. The redox cycle $Co^{2+} + Cu^{2+} \leftrightarrow Co^{3+} + Cu^{+}$ may be the main reason for the formation of Cu^{+2}. According to **Table 4**, the ratio of Cu^{1+}/Cu^{2+} increased when either the amount of Cu or Sr was enhanced. For Sr 3d in **Fig. 4**, Sr $3d_{5/2}$ spectra were deconvoluted into two contributions located at 131.9 and 133.6 eV. The first peak at low binding energy is attributed to Sr in the perovskite lattice while the one at high binding energy is due to Sr surface species [30]. According to **Table 4**, addition of either Cu or Sr caused an increase of the Sr_{seg}/S_{tot} ratio.

The relevant spectra of Co 2p in **Fig. 5** shows two main peaks at 779.7 eV (Co 2p3/2) and 794.9 eV (Co 2p1/2) as the signals of Co^{3+}, while the small peaks at 781.8 eV (Co 2p3/2) and 796.8 eV (Co 2p1/2) are due to Co^{2+} [22, 28]. For $La_{0.9}Sr_{0.1}Co_{1-y}Cu_yO_3$ samples, the acquired results in **Table 4** show that the ratio of Co^{2+}/Co^{3+} decreased as the amount of Cu enhanced. The formation of Co^{2+} in these cases is probably related to the redox cycle $Co^{2+} + Cu^{2+} \leftrightarrow Co^{3+} + Cu^{+}$ [21]. As Cu^{2+} ions are substituted at Co^{3+} sites, some Co^{2+} must be oxidized to Co^{3+} to maintain electrical neutrality, so the ratio of Co^{2+}/Co^{3+} decreases [5]. For $La_{1-x}Sr_xCo_{0.75}Cu_{0.25}O_3$ samples, the ratio of Co^{2+}/Co^{3+} slightly decreased as the amount of Sr enhanced. This behavior indicates that charge compensation in $La_{1-x}Sr_xCo_{0.75}Cu_{0.25}O_3$ samples seems to be slightly accomplished by the oxidation of Co^{2+} to Co^{3+} alongside the formation of oxygen vacancies.

From **Fig. 6**, two peaks at binding energies of 528.7 and 531.5 eV are observed which are attributed to lattice oxygen bonded to cations in the crystal structure (O_{latt}, e.g. O^{2-}) and adsorbed oxygen species (O_{ads}, e.g. O_2^-), respectively. The adsorbed oxygen species are mainly associated with surface defects such as oxygen vacancies [17, 22]. As given in **Table 4**, the ratio of O_{ads}/O_{latt} increased when the doping degree of either Cu or Sr enhanced, indicating the formation of oxygen defect sites due to the inhomogeneous distribution of oxygen after the deformation of perovskites. These results are in good agreement with those of H_2-TPR, where the area of α-reduction peaks to β-reduction peaks increased after the addition of either Sr or Cu into the $LaCoO_3$

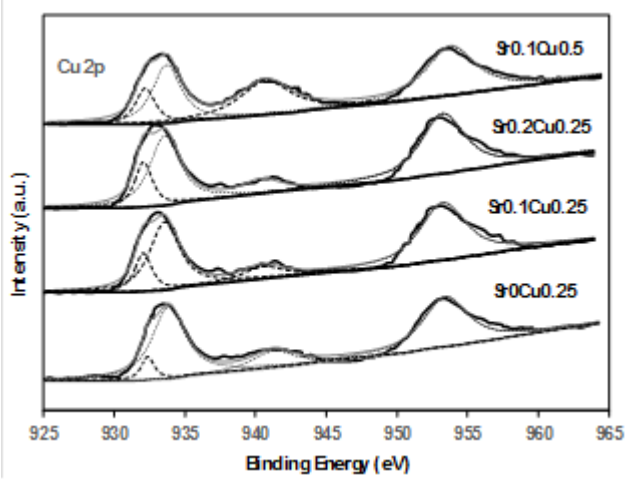

Fig. 3. Cu 2p XPS spectra of the perovskites.

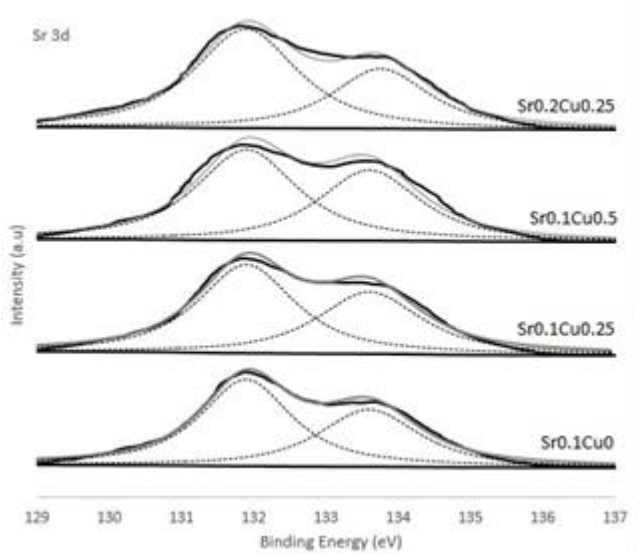

Fig. 4. Sr 3d XPS spectra of the perovskites.

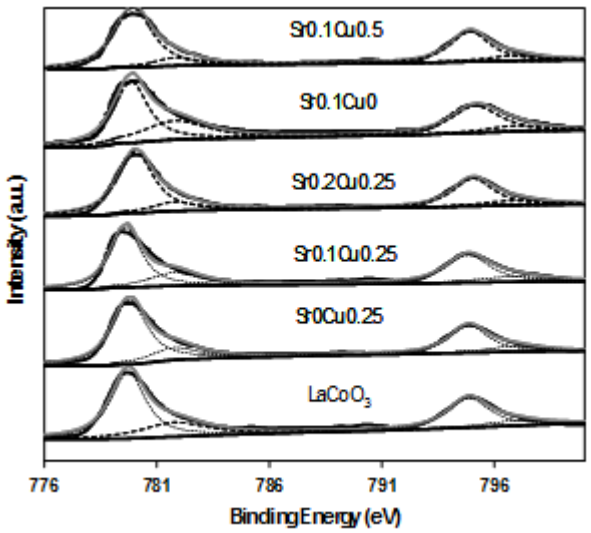

Fig. 5. Co 2p XPS spectra of the perovskites.

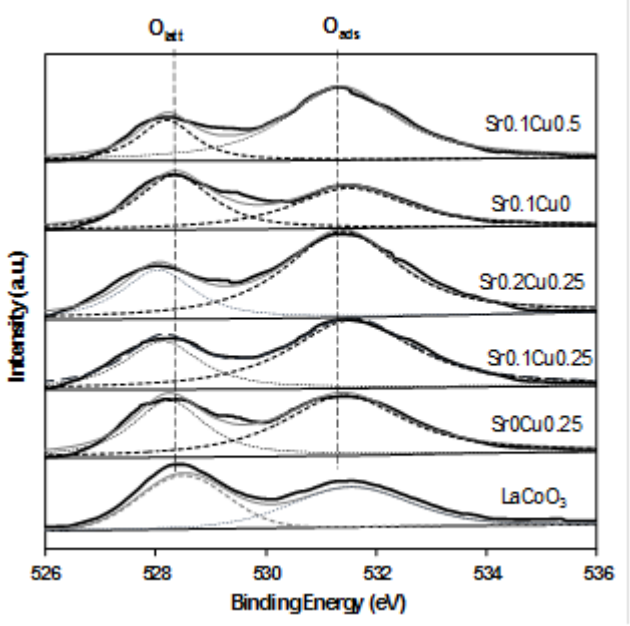

Fig. 6. O 1s XPS spectra of the perovskites.

structure. Furthermore, the first peak attributed to the lattice oxygen species shifted to lower binding energies as the amount of either Cu or Sr enhanced, implying these oxygen species became more mobile. The formation oxygen defects after the incorporation of Cu and Sr adsorbs gaseous oxygen and creates chemisorbed oxygen species through catching electrons, leading to the movement and transformation of the adsorbed and lattice oxygen species [26]. These behaviors are in good accordance with the movement of reduction peaks to lower temperatures in the TPR results.

3.2. Catalytic results and analysis of data

The catalytic activity of the elaborated perovskites in methane total combustion in the temperature range of 350-750 °C is given in **Fig. 7**. For comparison of catalytic activities, the activation energies were calculated using the Arrhenius equation. The design matrix obtained by the full factorial design and their corresponding activation energies are given in Table 5. Analysis of variance (ANOVA) was employed to evaluate the effects of the process variables (Cu and Sr) and their interactions on the activation energies (**Table 6**).

F-test and P-value were employed to examine the obtained model, standard residual/ error, and significance of each parameter. The F-test is defined as the ratio of the mean square (MS) to the residual mean square (MSresid). MS is the mean square of the factors or interactions while MSresid is the mean square of errors. The p-value is the probability of rejecting the null hypothesis of a study question, assuming that the null

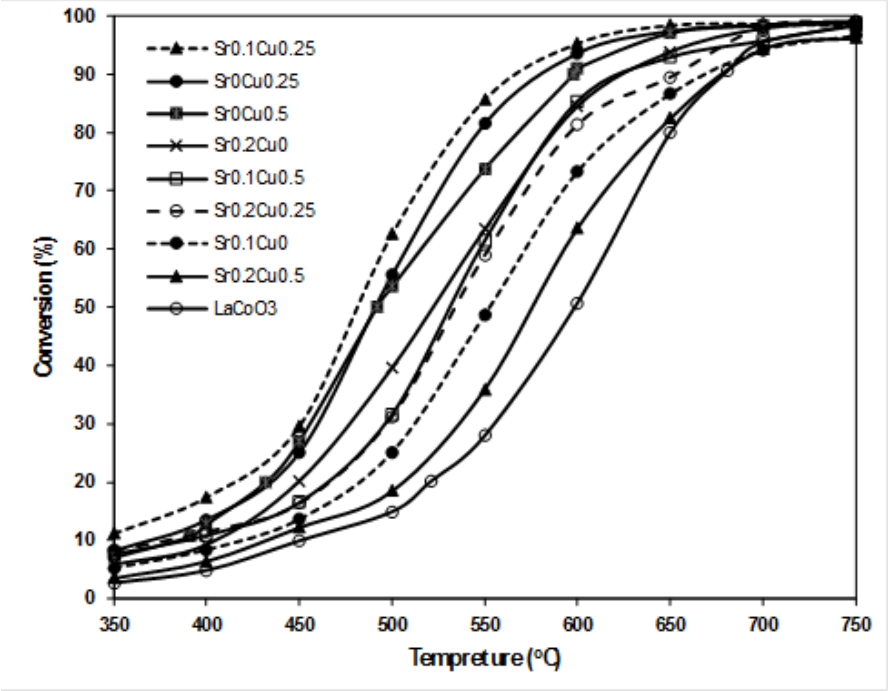

Fig. 7. Methane conversion over the perovskites as a function of temperature.

Table 6. Analysis of variance for the activation energy from the experimental design

Source	Sum of squares	Degree of freedom	Mean Square	F-value	p-value
Model	166.65	5	33.33	38.52	0.0064
A-Cu	14.54	1	14.54	16.80	0.0263
B-Sr	5.49	1	5.49	6.35	0.0862
AB	31.98	1	31.98	36.96	0.0089
A^2	64.90	1	64.90	75.00	0.0032
B^2	49.73	1	49.73	57.47	0.0048

hypothesis is correct. The smaller the p-value, the stronger evidence against the hypothesis. In statistical studies, a large F-test value with a p-value less than 0.05 indicates that a term is significant at 95% confidence limit [19, 31].

From ANOVA results, the F-test value of 38.52 and the p value of 0.0064 mean that the model is statistically significant and can estimate the activation energy with Cu and Sr doping degrees as the variables. Furthermore, factor A and interactions AB, A^2 and B^2 with p-values less than 0.05 are statistically significant.

A quadratic equation for the activation energy as the function of actual variables was obtained as follows:

$$Activation\ Energy\ (kJ/mol) = 69.78 - 63.11 \times Cu - 137.57 \times Sr + 113.10 \times Cu \times Sr + 91.14 \times Cu^2 + 498.66 \times Sr^2 \quad \textbf{(3)}$$

where Cu and Sr are substitution degrees. The correlation coefficient (R^2) of **Eq. 3** is 0.959, representing a fitting with high accuracy for the model. Moreover, the linear distribution of the experimental points along the idealized trend in **Fig. 8** indicates that the deviations of predicted values from experimental values are low.

3.2.1 Response surface (contour) plots and Interactions effects

Eq. 3 was employed to obtain a contour plot for the activation energy as a function of Cu and Sr doping degrees. The acquired results are shown in **Fig. 9**. The contour plot is a graphical representation of **Eq. 3**. As shown in **Fig. 9**, the activation energy decreases with the simultaneous increase of Cu and Sr doping degrees up to the range of 0.07-0.15 for Sr and 0.2-0.4 for Cu. In this range, the activation energy is about 54 kj/mol. It can be observed that at high levels of Cu and Sr doping degrees, the activation energy is high.

Two-factor interaction plot (**Fig. 10**) can also provide useful information about the interaction of Cu and Sr doping degrees (A × B). According to **Fig. 10**, at the lowest Sr doping degree (Sr=0), the activation energy decreased from about 70 to 61 kj/mol when Cu doping

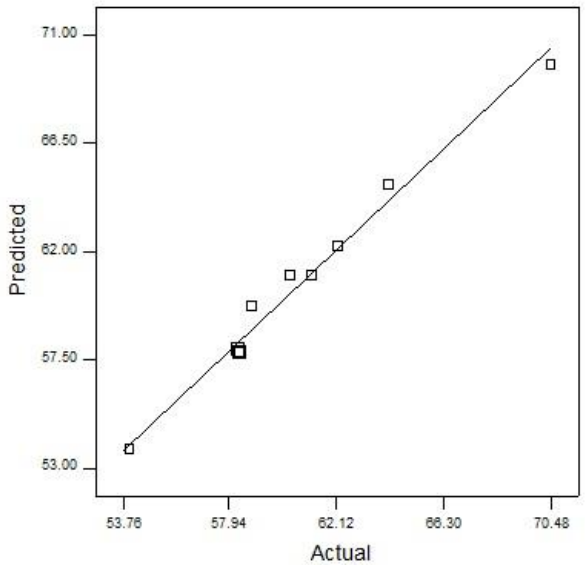

Fig. 8. Predicted vs. actual values for activation energy.

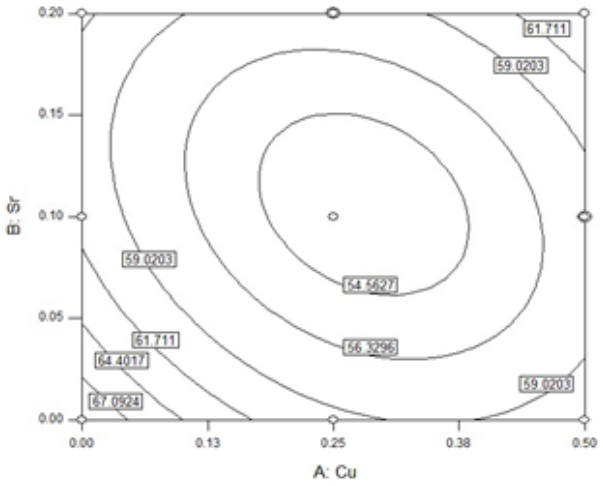

Fig. 9. Contour plot describing the response surface for activation energy as a function of Cu vs. Sr doping degrees.

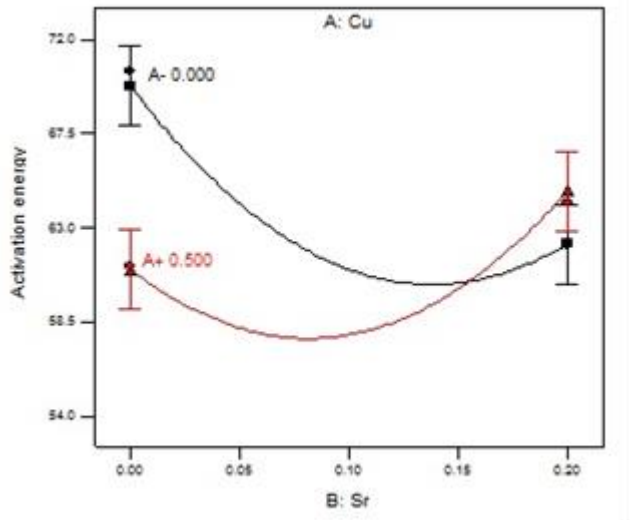

Fig. 10. Interaction effect of A × B on the activation energy.

degree increased from 0 to 0.5. However, the effect of Cu doping degree became weaker at superior Sr doping degree. For instance, the effect of Cu doping degree was negligible when factor B (Sr doping degree) was set at about 0.15. Further increasing of factor B from 0.15 caused an inverse effect on the activation energy so that the activation energy increased when Cu doping degree increased. On the other hand, at the high level of Cu doping degree, increasing Sr doping degree brings about a minimum value of the activation energy at Sr doping degree =0.08 while at the low level of Cu doping degree, increasing Sr doping degree led to a nearly continuous decrease of the activation energy. These behaviors demonstrate that there is a limited capacity for $LaCoO_3$ to accommodate Sr and Cu into the lattice aiming at improving the catalytic combustion activity.

The incorporation of Cu and Sr into the $LaCoO_3$ structure altered crystallinity, BET specific surface area, reducibility, oxygen mobility and oxygen vacancies. It was observed from XRD results that the incorporation of Cu and Sr decreased crystallinity and led to segregation of some oxide phases at high levels of Cu and Sr doping degrees. This segregation of oxide phases caused reduction in the BET specific surface area due to blockage of access to some pores. Therefore, the main reason for the deterioration of the activity at high levels of Cu and Sr doping degrees was due to the decrease in crystallinity and BET specific surface area.

Partial substitution of La^{+3} by Sr^{+2} and Co^{+3} by Cu^{+2} in $LaCoO_3$ structure resulted in the formation of positive charge defects. It is suggested that these defects are balanced by the formation of oxygen vacancies (adsorbed oxygen species), as evidenced by O1s XPS, where it is observed that the O_{ads} /O_{latt} ratio increases at elevated doping degrees of either Cu or Sr. It is known that adsorbed oxygen species are more active compared to lattice oxygen species due to higher accessibility and mobility [32]. The existence of more oxygen vacancies accelerated the oxygen mobility and increased oxygen capacity, so the reducibility in α-reduction region improved, as revealed by H_2-TPR results. Higher oxygen mobility, oxygen capacity and reducibility facilitated oxygen accessibility to methane and accordingly resulted in higher activity.

Apart from oxygen vacancies, lattice oxygen species also play important roles in oxidation of methane. According to Mars-Van-Krevelen mechanism, after adsorption and dissociation of O_2 molecules on the perovskite surface, they are incorporated into the crystal lattice of perovskite as O^2 species and then are utilized in the oxidation reaction [33]. As indicated by H_2-TPR results, addition of either Sr or Cu into the $LaCoO_3$ enhanced and eased reducibility in the β-reduction

region. On the other hand, O1s XPS results showed that the mobility of lattice oxygen species improved after the incorporation of either Sr or Cu. The improved reducibility, oxygen capacity and oxygen mobility of lattice oxygen accelerate the movement of lattice oxygen from interior to surface and make them accessible to methane.

The difference in electronegativity of Cu (1.90) and Co (1.88) is another factor which could effect on metal-oxygen binding interaction. The smaller difference in electronegativity between Cu and oxygen compared to Co and oxygen weakens the interaction of oxygen to Cu sites. This further proves our XPS results where it was observed that the oxygen mobility enhanced after incorporation of Cu into $LaCoO_3$ lattice. The weakened metal-oxygen binding interaction activates C-H bond of methane more easily, leading to higher activity [25].

Many reports on oxidation of methane over perovskite based catalysts can be found in literature and we have summarized some of the best reported results in **Table 7**. $LaAl_{0.9}Pd_{0.1}O_3$ by Yang et al. [34] stands out because of its lower T_{90} (reaction temperature for 90% conversion of methane). Experiments in the present study have been obtained under most unfavorable reaction conditions, i.e. GHSV = 64000 h^{-1} and CH_4 = 2 vol.% in the feed stream, resulting in higher T_{90}. Despite more unfavorable reaction conditions as compared to the literature results in **Table 7**, comparable results have been achieved in this work.

Table 7. Summarized perovskite-based catalysts for methane combustion

catalyst	Feedstream (vol%)	GHSV, h^{-1}	T_{90}	Ref.
$La_{0.6}Sr_{0.4}MnO$	0.25% CH_4, 1% Ne, balance O_2	5625	480	[33]
$LaCo_{0.8}Fe_{0.2}O_3$	0.25% CH_4, 1% Ne, balance O_2	5625	490	[4]
$La_{0.75}Ag_{0.25}FeO_3$	1% CH_4, balance air	5800	475	[23]
$BaCe_{0.6}Mn_{0.4}O_3$	1% CH_4, balance air	20L·g^{-1}·h^{-1}	423	[35]
$LaAl_{0.9}Pd_{0.1}O_3$	1% CH_4, 20% O_2, balance N_2	15L·g^{-1}·h^{-1}	400	[34]
$La_{0.9}Sr_{0.1}Co_{0.75}Cu_{0.25}O_3$	2% CH_4, 18% O_2, balance N_2	64000	550	This work

4. Conclusions

The catalytic performance of $La_{1-x}Sr_xCo_{1-y}Cu_yO_3$ perovskites was optimized by changing Sr and Cu doping degrees using full factorial deign of experiment. The substitution of Sr^{+2} at La^{+3} sites and Cu^{+2} at Co^{+3} sites led to the formation of charge imbalances which was subsequently compensated by the creation of oxygen vacancies. Although these substitutions decreased the crystallinity, the catalytic activity enhanced in combustion of methane. Formation of oxygen vacancies increased oxygen capacity, oxygen mobility and reducibility which accordingly enhanced exchange capacity between lattice oxygen and gas phase oxygen. A minimum in the activation energy was observed by increase of Sr and Cu doping degrees at moderate values of the corresponding parameters. The best performance belonged to Sr0.1Cu0.25 with activation energy of 54.02 kj/mol. The segregation of oxide phases and decrease of BET specific surface area were the main reasons for the deterioration of activity at high levels of Sr and Cu doping degrees.

References

[1] R. Hu, R. Ding, J. Chen, J. Hu, Y. Zhang, Preparation and catalytic activities of the novel double perovskite-type oxide La_2CuNiO_6 for methane combustion, Catal. Commun., 21 (2012) 38-41.

[2] L. Marchetti, L. Forni, Catalytic combustion of methane over perovskites, Appl. Catal. B: Environ., 15 (1998) 179-187.

[3] R.J. Liu, P.A. Crozier, C.M. Smith, D.A. Hucul, J. Blackson, G. Salaita, Metal sintering mechanisms and regeneration of palladium/alumina hydrogenation catalysts, Appl. Catal. A, 282 (2005) 111-121.

[4] S. Royer, F. Berube, S. Kaliaguine, Effect of the synthesis conditions on the redox and catalytic properties in oxidation reactions of $LaCo_{1-x}FexO_3$, Appl. Catal. A, 282 (2005) 273-284.

[5] J. Yang, Y. Guo, Nanostructured perovskite oxides as promising substitutes of noble metals catalysts for catalytic combustion of methane, Chin. Chem. Lett., 29 (2018) 252-260.

[6] G. Zou, M. Chen, W. Shangguan, Promotion effects of $LaCoO_3$ formation on the catalytic performance of Co–La oxides for soot combustion in air, Catal. Commun., 51 (2014) 68-71.

[7] I. Rossetti, L. Forni, Catalytic flameless combustion of methane over perovskites prepared by flame–hydrolysis, Appl. Catal. B: Environ., 33 (2001) 345-352.

[8] G. Pecchi, C. Campos, O. Peña, L.E. Cadus, Structural, magnetic and catalytic properties of perovskite-type mixed oxides $LaMn_{1-y}Co_yO_3$ (y= 0.0, 0.1, 0.3, 0.5, 0.7, 0.9, 1.0), J. Mol. Catal. A: Chem., 282 (2008) 158-166.

[9] D. Maiti, Y.A. Daza, M.M. Yung, J.N. Kuhn, V.R. Bhethanabotla, Oxygen vacancy formation characteristics in the bulk and across different surface terminations of $La_{(1-x)}Sr_xFe_{(1-y)}Co_yO_{(3-\delta)}$ perovskite oxides for CO_2 conversion, J. Mater. Chem. A, 4 (2016) 5137-5148.
[10] J. Chen, M. Shen, X. Wang, J. Wang, Y. Su, Z. Zhao, Catalytic performance of NO oxidation over $LaMeO_3$ (Me= Mn, Fe, Co) perovskite prepared by the sol–gel method, Catal. Commun., 37 (2013) 105-108.
[11] E. Campagnoli, A. Tavares, L. Fabbrini, I. Rossetti, Y.A. Dubitsky, A. Zaopo, L. Forni, $La_{1-x}A_xCo_{1-y}Fe_yO_{3\pm\delta}$(A′= Ce, Sr) catalysts for the flameless combustion of methane, J. Mater. Sci., 41 (2006) 4713-4719.
[12] Y. Wu, L. Li, B. Chu, Y. Yi, Z. Qin, M. Fan, Q. Qin, H. He, L. Zhang, L. Dong, Catalytic reduction of NO by CO over B-site partially substituted $LaM_{0.25}Co_{0.75}O_3$ (M= Cu, Mn, Fe) perovskite oxide catalysts: The correlation between physicochemical properties and catalytic performance, Appl. Catal. A: General, 568 (2018) 43-53.
[13] A. Glisenti, M. Pacella, M. Guiotto, M.M. Natile, P. Canu, Largely Cu-doped $LaCo_{1-x}CuxO_3$ perovskites for TWC: Toward new PGM-free catalysts, Appl. Catal. B: Environ., 180 (2016) 94-105.
[14] H. Rezaei Shadegan, S. Maghsoodi, B. Ghanavati, A. Shahbazi Kootenaei, A. Azimi, Catalytic combustion of methane over La2BCoO6 perovskites containing Ni, Cu and Fe: impact of B-sites on oxygen species and catalytic activity, Reac. Kin., Mech. Catal., 131 (2020) 737-752.
[15] Z. Wang, R. Peng, W. Zhang, X. Wu, C. Xia, Y. Lu, Oxygen reduction and transport on the $La_{1-x}Sr_xCo_{1-y}Fe_yO_{3-\delta}$ cathode in solid oxide fuel cells: A first-principles study, J. Mater. Chem. A, 1 (2013) 12932-12940.
[16] C.H. Kim, G. Qi, K. Dahlberg, W. Li, Strontium-doped perovskites rival platinum catalysts for treating NOx in simulated diesel exhaust, Science, 327 (2010) 1624-1627.
[17] L. Zhang, Y. Zhang, H. Dai, J. Deng, L. Wei, H. He, Hydrothermal synthesis and catalytic performance of single-crystalline $La_{2-x}Sr_xCuO_4$ for methane oxidation, Catal. Today, 153 (2010) 143-149.
[18] N. Tien-Thao, H. Alamdari, M. Zahedi-Niaki, S. Kaliaguine, $LaCo_{1-x}Cu_xO_{3-\delta}$ perovskite catalysts for higher alcohol synthesis, Appl. Catal. A, 311 (2006) 204-212.
[19] A.Z. Varzaneh, M.S. Moghaddam, J.T. Darian, Oxidative dehydrogenation of propane over vanadium catalyst supported on nano-HZSM-5, Petrol. Chem., 58 (2018) 13-21.
[20] A.Z. Varzaneh, A.H.S. Kootenaei, J. Towfighi, A. Mohamadalizadeh, Optimization and deactivation study of Fe–Ce/HZSM-5 catalyst in steam catalytic cracking of mixed ethanol/naphtha feed, J. Anal. Appl. Pyrol., 102 (2013) 144-153.
[21] Y. Wu, B. Chu, M. Zhang, Y. Yi, L. Dong, M. Fan, G. Jin, L. Zhang, B. Li, Influence of calcination temperature on the catalytic properties of $LaCu_{0.25}Co_{0.75}O_3$ catalysts in NO_x reduction, Appl. Surf. Sci., 481 (2019) 1277-1286.
[22] J.A. Onrubia, B. Pereda-Ayo, U. De-La-Torre, J.R. González-Velasco, Appl. Catal. B: Environ., 213 (2017) 198-210.
[23] B. Kucharczyk, K. Adamska, W. Tylus, W. Miśta, B. Szczygieł, J. Winiarski, Effect of Silver Addition to $LaFeO_3$ Perovskite on the Activity of Monolithic $La_{1-x}Ag_xFeO_3$ Perovskite Catalysts in Methane Hexane Oxidation, Catal. Lett., 149 (2019) 1919-1933.
[24] B. Kucharczyk, W. Tylus, Metallic monolith supported $LaMnO_3$ perovskite-based catalysts in methane combustion, Catal. Lett., 115 (2007) 122-132.
[25] K. Sutthiumporn, T. Maneerung, Y. Kathiraser, S. Kawi, CO_2 dry-reforming of methane over $La_{0.8}Sr_{0.2}Ni_{0.8}M_{0.2}O_3$ perovskite (M = Bi, Co, Cr, Cu, Fe): Roles of lattice oxygen on C–H activation and carbon suppression, Int. J. Hyd. En., 37 (2012) 11195-11207.
[26] Y. Wu, G. Li, B. Chu, L. Dong, Z. Tong, H. He, L. Zhang, M. Fan, B. Li, L. Dong, NO Reduction by CO over Highly Active and Stable Perovskite Oxide Catalysts $La_{0.8}Ce_{0.2}M_{0.25}Co_{0.75}O_3$ (M = Cu, Mn, Fe): Effect of the Role in B Site, Indust. Eng. Chem. Res., 57 (2018) 15670-15682.
[27] G. Valderrama, A. Kiennemann, M.R. Goldwasser, La-Sr-Ni-Co-O based perovskite-type solid solutions as catalyst precursors in the CO_2 reforming of methane, J. Power Sourc., 195 (2010) 1765-1771.
[28] S.S. Maluf, E.Y. Tanabe, P.A.P. Nascente, E.M. Assaf, Study of Water–Gas-Shift Reaction over $La_{(1-y)}Sr_yNi_xCo_{(1-x)}O_3$ Perovskite as Precursors, Topics in Catal., 54 (2011) 210-218.
[29] C. Deng, Q. Huang, X. Zhu, Q. Hu, W. Su, J. Qian, L. Dong, B. Li, M. Fan, C. Liang, Appl. Surf. Sci., 389 (2016) 1033-1049.
[30] E.J. Crumlin, E. Mutoro, W.T. Hong, M.D. Biegalski, H.M. Christen, Z. Liu, H. Bluhm, Y. Shao-Horn, In Situ Ambient Pressure X-ray Photoelectron Spectroscopy of Cobalt Perovskite Surfaces under Cathodic Polarization at High Temperatures, J. Physic. Chem. C, 117 (2013) 16087-16094.
[31] A.Z. Varzaneh, J. Towfighi, A.H.S. Kootenaei, A. Mohamadalizadeh, Effect of cerium and zirconium nanoparticles on the structure and catalytic performance of SAPO-34 in steam cracking of naphtha to light olefins, React. Kin., Mech. Catal., 115 (2015) 719-740.
[32] Y. Zheng, K. Li, H. Wang, D. Tian, Y. Wang, X. Zhu, Y. Wei, M. Zheng, Y. Luo, Designed oxygen carriers from macroporous $LaFeO_3$ supported CeO_2 for chemical-looping reforming of methane, Appl. Catal. B: Environ., 202 (2017) 51-63.
[33] S. Royer, H. Alamdari, D. Duprez, S. Kaliaguine, Oxygen storage capacity of $La_{1-x}A'_xBO_3$ perovskites (with A′= Sr, Ce; B= Co, Mn)—relation with catalytic activity in the CH_4 oxidation reaction, Appl. Catal. B: Environ., 58 (2005) 273-288.
[34] X. Yang, Q. Gao, Z. Zhao, Y. Guo, Y. Guo, L. Wang, Y. Wang, W. Zhan, Surface tuning of noble metal doped perovskite oxide by synergistic effect of thermal treatment and acid etching: A new path to high-performance catalysts for methane combustion, Appl. Catal. B: Environ., 239 (2018) 373-382.
[35] X. Tan, N. Han, H. Chen, L. Su, C. Zhang, Y. Li, Investigation of perovskite $BaCe_{1-x}MnxO_{3-\delta}$ for methane combustion, Ceram. Int., 47 (2020) 8762-8768.